ROYAL SOCIETY
OF CHEMISTRY

COMMUNICATION

View Article Online
View Journal | View Issue

Confined growth of pyridinic N–Mo_2C sites on MXenes for hydrogen evolution†

Hao Wang, [ID] ‡[a] Yanping Lin,‡[b] Shuyuan Liu,‡[b] Jianmin Li,[ID][c] Liangmin Bu,[b] Jianmei Chen,[d] Xu Xiao, [ID] *[e] Jin-Ho Choi,[ID][b] Lijun Gao [ID] *[b] and Jong-Min Lee [ID] *[a]

Developing low-cost and high-performance hydrogen evolution reaction (HER) electrocatalysts is a key research area for scalable hydrogen production from water electrolysis. Here, a hybrid of nitrogen-doped carbon encapsulated Mo_2C nanodots on $Ti_3C_2T_x$ MXene ($Mo_2C/Ti_3C_2T_x$@NC) is developed through *in situ* polymerization of dopamine and a Mo precursor on the $Ti_3C_2T_x$ MXene surface. During the annealing treatment, the polydopamine plays multiple roles in forming N-doped carbon, confining MoO_4^{2-} ions into ultrasmall Mo_2C nanodots, and stabilizing the MXene flakes against spontaneous oxidation. The as-synthesized hybrid exhibits excellent HER activity in acidic electrolyte with an overpotential of 53 mV at 10 mA cm^{-2} and excellent stability over 30 hours. The combination of experiments and simulations demonstrates that pyridinic N-doped carbon coated Mo_2C nanodots serve as the active sites and $Ti_3C_2T_x$ MXene facilitates the charge transfer, synergistically contributing to the superior HER performance.

Owing to the high energy density and zero carbon emission, hydrogen is considered as an optimal solution to address the energy crisis and alleviate the environmental pollution.[1,2] Although industrial hydrogen production still relies on fossil fuels, water electrolysis shows promise as a clean and sustainable route for hydrogen generation.[3,4] Thus, developing efficient hydrogen evolution reaction (HER) electrocatalysts is of great

importance to realize scalable electrocatalytic hydrogen production. Until now, platinum (Pt) and its derivatives remain the best HER electrocatalysts with low overpotentials and fast reaction kinetics, but their low abundance and high cost severely hinder their large-scale use.[5] Recently, intensive research efforts have been made to explore low-cost and earth-abundant alternatives with comparable HER performance.[6–15] Among them, molybdenum carbide (Mo_2C) holds great promise due to its Pt-like d-band electronic structure.[16] In general, the HER activity of Mo_2C mainly relies on the accessibility of active sites and conductivity. Mo_2C nanoparticles, even ultrasmall nanodots, are preferable but tend to agglomerate when processed into electrodes. In this context, introducing a highly conductive substrate that could simultaneously optimize the dispersion of ultrasmall Mo_2C would be of importance.[17,18]

Recently, an emerging family of two-dimensional (2D) transition metal carbides and nitrides, called MXenes, have attracted much attention due to their unique characteristics of metallic conductivity (up to 10 000 S cm^{-1}), hydrophilicity and diversity stemming from various surface terminations.[19,20] Typically, the most studied $Ti_3C_2T_x$ MXene (T_x denotes the surface –OH, –O and –F groups) shows great promise in various applications including supercapacitors,[21] sensors,[22] water purification,[23] electromagnetic interference shielding[24] and catalysis.[25–29] It would be natural to assume that coupling Mo_2C and MXenes may deliver satisfactory HER performance, while it remains challenging due to the following factors. First, the synthesis of Mo_2C always requires high annealing temperature. Proverbially, MXenes with high surface energy are prone to oxidation at evaluated temperatures, although protected by an inert atmosphere, leading to inferior conductivity.[30] In addition, the high synthesis temperature would accelerate the agglomeration of Mo_2C nanoparticles and thus result in poor accessibility of active sites.[31] Accordingly, protecting MXenes from surface oxidization and Mo_2C nanoparticles from aggregation during the calcination process is of great importance to realize MXene–Mo_2C hybrid HER electrocatalysts.

[a]*School of Chemical and Biomedical Engineering, Nanyang Technological University, Singapore 637459, Singapore. E-mail: jmlee@ntu.edu.sg*

[b]*Soochow Institute for Energy and Materials Innovations, College of Energy, Soochow University, Suzhou 215006, China. E-mail: gaolijun@suda.edu.cn*

[c]*Department of Materials Science and Engineering, National University of Singapore, Singapore 117576, Singapore*

[d]*Institute of Functional Nano and Soft Materials (FUNSOM), Jiangsu Key Laboratory for Carbon-Based Functional Materials & Devices, Soochow University, Suzhou 215123, China*

[e]*A.J. Drexel Nanomaterials Institute and Department of Materials Science and Engineering, Drexel University, Philadelphia, 19104, USA. E-mail: xx58@drexel.edu*

‡ These authors contributed equally to this work.

This journal is © The Royal Society of Chemistry 2020

J. Mater. Chem. A, 2020, 8, 7109–7116 | **7109**

Here, we report a 2D coupled nanohybrid of Mo_2C nanodots and $Ti_3C_2T_x$ MXene encapsulated by nitrogen-doped carbon layers (denoted as $Mo_2C/Ti_3C_2T_x$@NC) synthesized using molybdate ions chelated in polydopamine (Mo-PDA) as the precursor (Fig. 1). Notably, $Ti_3C_2T_x$ flakes are fully capped with Mo-PDA by *in situ* polymerization, which could inhibit the surface oxidation of $Ti_3C_2T_x$ during annealing treatment and thus retain the excellent conductivity.[32] Moreover, due to the confinement effect of the Mo-PDA structure, the ultrasmall Mo_2C nanodots are uniformly dispersed in the carbon matrix without agglomeration. Demonstrated by theoretical and experimental analyses, the highly accessible pyridinic $N–Mo_2C$ sites coupled with the metallic $Ti_3C_2T_x$ support of $Mo_2C/Ti_3C_2-T_x$@NC can deliver remarkable HER activities with an overpotential of 53 mV at 10 mA cm^{-2}, a Tafel slope of 40 mV dec^{-1} and excellent stability over 30 hours in acidic electrolyte, which are superior to those of reported noble metal-free electrocatalysts.

As demonstrated previously, PDA may have a positive confinement effect on the dispersion of Mo_2C nanodots, in which a hierarchical microflower carbon structure was formed (Fig. S1†). Even though Mo_2C nanodots may be well dispersed, such a microflower structure would show inferior HER performance in terms of low conductivity. We assume that 2D $Ti_3C_2T_x$ MXene with various terminations may be a good candidate as a metallically conductive substrate to form a flat PDA layer, realizing both well dispersed Mo_2C nanodots and fast electron transport. To verify this idea, we first check the morphology of polydopamine on the MXene by *in situ* polymerization. The ultrathin $Ti_3C_2T_x$ with a lateral size of several microns exhibits single crystallinity (Fig. S2†). By *in situ* polymerization of dopamine on the surface of $Ti_3C_2T_x$ MXene, the polydopamine/$Ti_3C_2T_x$ (denoted as PDA/$Ti_3C_2T_x$) shows a similar morphology to the pristine MXene (Fig. 2a). After annealing at 750 °C, the pristine MXene is severely oxidized with many TiO_2 nanoparticles/nanorods generated on the surface (Fig. S3a†), while the N-doped carbon coated $Ti_3C_2T_x$ MXene (denoted as $Ti_3C_2T_x$@NC) derived from PDA/$Ti_3C_2T_x$ retains the flat surface without the presence of TiO_2 particles (Fig. 2b), which is confirmed from the enlarged TEM image (Fig. S3b†). The high-resolution TEM (HRTEM) image (Fig. 2c) clearly shows that the $Ti_3C_2T_x$ MXene layers are fully covered by carbon.

The structures of these samples were further investigated by X-ray diffraction (XRD) and Raman spectroscopy. The pristine MXene exhibits the typical peak at ~7° corresponding to the (002) plane of $Ti_3C_2T_x$ MXene (Fig. S4a†).[23] The (002) peak of PDA/$Ti_3C_2T_x$ shifts to ~6° due to the expanded interlayer spacing of $Ti_3C_2T_x$ layers. The annealed pristine MXene does not show characteristic $Ti_3C_2T_x$ MXene peaks but shows typical peaks of rutile TiO_2 (JCPDS no. 21-1276).[34] Notably, no TiO_2 peaks are observed in the $Ti_3C_2T_x$@NC XRD pattern. In addition, the (002) peak of $Ti_3C_2T_x$ MXene disappeared, which should be attributed to the suppressed restacking of MXene flakes by carbon layers on the surface.[35] The Raman spectra (Fig. S4b†) show that all the pristine $Ti_3C_2T_x$, PDA/$Ti_3C_2T_x$ and $Ti_3C_2T_x$@NC samples exhibit typical peaks corresponding to $Ti_3C_2T_x$ MXene while annealed $Ti_3C_2T_x$ shows the characteristic peaks at 237.7, 446.9 and 609.8 cm^{-1} of rutile TiO_2.[36] In addition, X-ray photoelectron spectroscopy (XPS) analyses (Fig. S5†) confirm the oxidation of $Ti_3C_2T_x$ MXene into TiO_2 during the annealing process. Based on the above results, it can be concluded that dopamine self-polymerized on the surface of the MXene could protect it from oxidation during the annealing treatment by *in situ* forming N-doped carbon layers.

Previous studies have reported that molybdate ions can react with dopamine and then polymerize into the Mo-PDA complex, which can be used to fabricate nanostructured Mo compound/carbon composites for various applications.[33,37,38] Based on this inspiration, here we prepared Mo-PDA/$Ti_3C_2T_x$ through a facile *in situ* polymerization method, as depicted in Fig. 1. The SEM and TEM images (Fig. S6†) of Mo-PDA/$Ti_3C_2T_x$ show a similar ultrathin morphology to PDA/$Ti_3C_2T_x$, confirming that $Ti_3C_2T_x$ flakes are tightly covered by Mo-PDA layers. $Mo_2C/Ti_3C_2T_x$@NC was obtained by annealing Mo-PDA/$Ti_3C_2T_x$ under Ar at 750 °C. As shown in Fig. 2d and Fig. S7,† the morphology of $Mo_2C/Ti_3C_2T_x$@NC is similar to that of $Ti_3C_2T_x$@NC (Fig. 2b). The enlarged TEM image (Fig. 2e) evidences that high-density ultrasmall Mo_2C nanodots with an average diameter of 1.1 nm (Fig. 2f) are uniformly anchored on the surface of $Ti_3C_2T_x$ flakes. The high-resolution TEM image (Fig. 2g) exhibits the lattice fringes of ~0.23 nm on the nanodots, corresponding to the *d*-spacing of the β-Mo_2C (101) plane.[17] The background lattices belong to $Ti_3C_2T_x$, confirming its hexagonal structure. The high-angle annular dark field scanning TEM (HAADF-STEM) image (Fig. 2h) reveals numerous bright dots
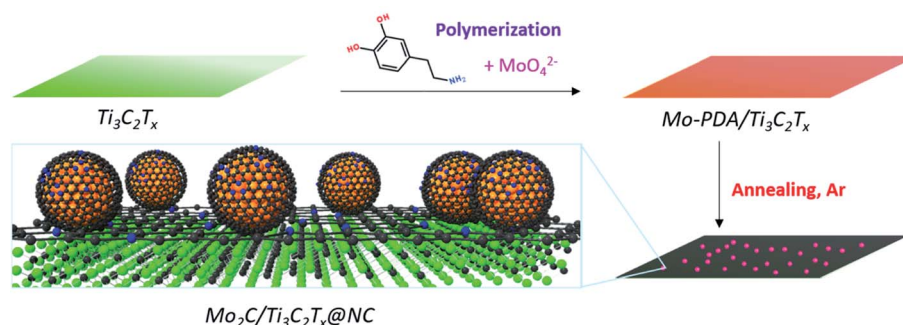

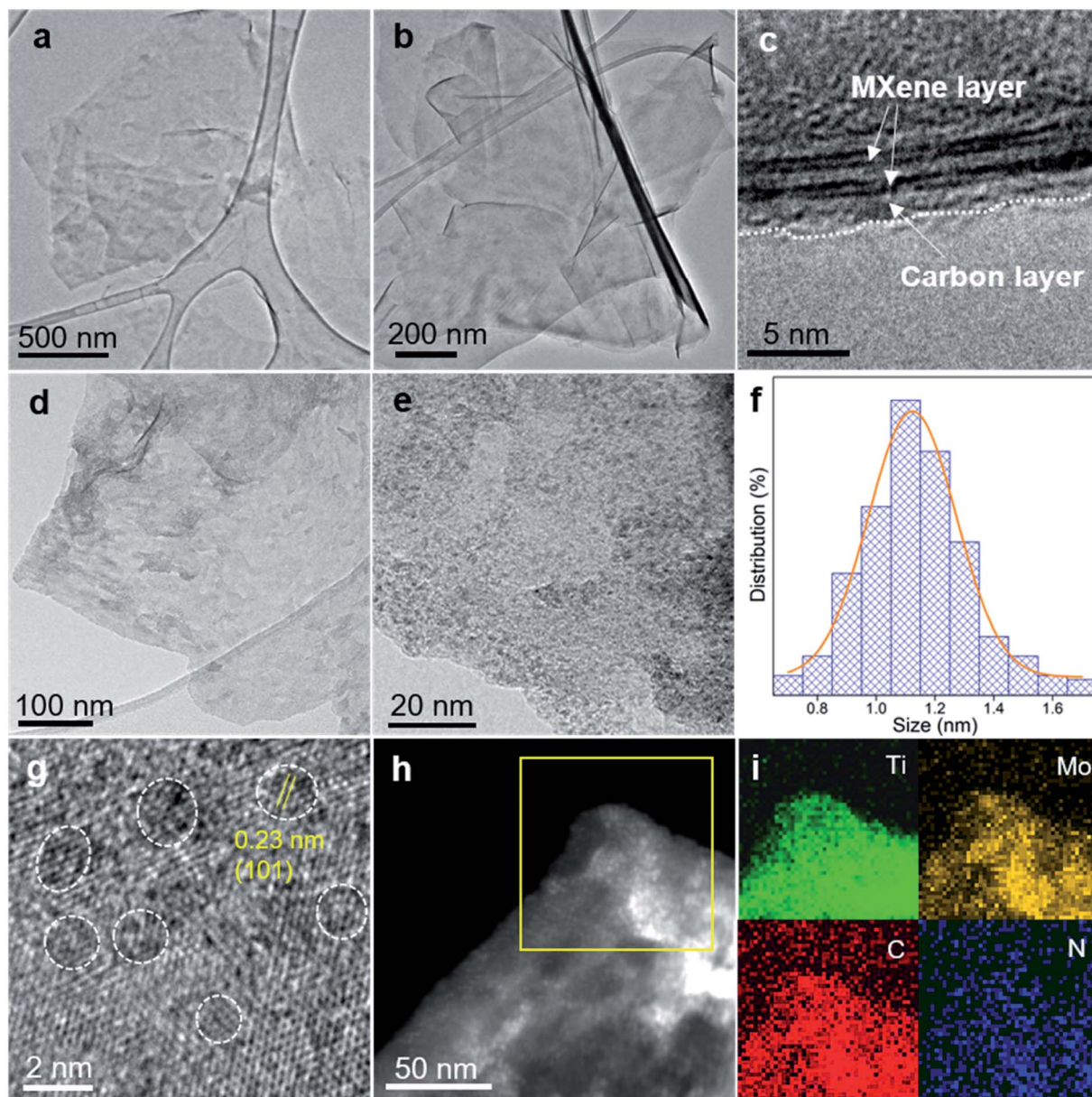**Fig. 1** Synthetic illustration of the preparation of $Mo_2C/Ti_3C_2T_x$@NC.

Fig. 2 TEM images of (a) PDA/$Ti_3C_2T_x$, (b) $Ti_3C_2T_x$@NC and (d) $Mo_2C/Ti_3C_2T_x$@NC. (c) HRTEM image of a $Ti_3C_2T_x$@NC edge showing the carbon layer covered $Ti_3C_2T_x$ MXene structure. (e) Enlarged TEM image of $Mo_2C/Ti_3C_2T_x$@NC showing the uniform dispersion of Mo_2C nanodots on the surface of $Ti_3C_2T_x$ MXene. (f) Size distribution of Mo_2C nanodots in $Mo_2C/Ti_3C_2T_x$@NC counted in (e). HRTEM image (g) and HAADF-STEM image (h) of $Mo_2C/Ti_3C_2T_x$@NC. (i) EDX elemental mapping from the marked region in (h).

decorated on the MXene sheets, further demonstrating the uniform dispersion of Mo_2C nanodots. The corresponding energy dispersive X-ray spectroscopy (EDX) elemental mapping images (Fig. 2i) confirm the distribution of Ti, Mo, C and N elements on the $Mo_2C/Ti_3C_2T_x$@NC surface.

Fig. 3a displays the XRD patterns of the samples. The characteristic peaks of both Mo-PDA and the MXene are observed in the XRD pattern of Mo-PDA/$Ti_3C_2T_x$. Similar to PDA/$Ti_3C_2T_x$, the (002) peaks of $Ti_3C_2T_x$ negatively shift due to the expanded interlayer spacing. The absence of the (002) peak in $Mo_2C/Ti_3C_2T_x$@NC results from the separation of MXene layers by the Mo_2C nanodots and carbon layers. Through investigation using

N$_2$ adsorption–desorption isotherms, as shown in Fig. 3b, the Brunauer–Emmett–Teller (BET) surface areas of $Mo_2C/Ti_3C_2T_x$@NC and Mo_2C@NC were calculated to be 241.4 and 86.4 m^2 g^{-1}, respectively. Both samples exhibit type IV isotherms of mesoporous structures, with pores in the range from 2 to 50 nm. The larger surface area and mesoporous structure of $Mo_2C/Ti_3C_2T_x$@NC could facilitate the accessibility of active sites and charge transfer during the HER process.

The valence states and compositions of $Mo_2C/Ti_3C_2T_x$@NC were elucidated by XPS analyses. The XPS full scan (Fig. S8a†) evidences the existence of Ti, Mo, C, N, and O in $Mo_2C/Ti_3C_2T_x$@NC. The Ti 2p core level can be fitted with four doublets for
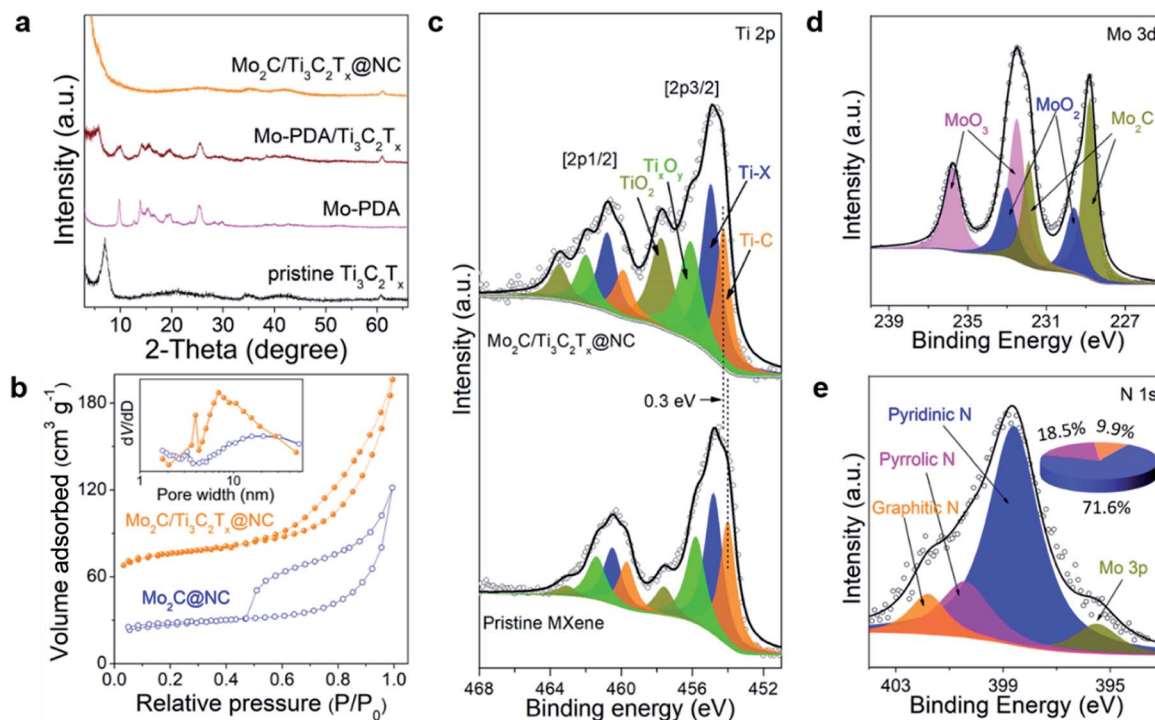
Fig. 3 (a) XRD patterns of pristine $Ti_3C_2T_x$ MXene, Mo-PDA, Mo-PDA/$Ti_3C_2T_x$ and Mo_2C/$Ti_3C_2T_x$@NC. (b) N_2 adsorption–desorption isotherms and the corresponding pore size distributions of Mo_2C@NC and Mo_2C/$Ti_3C_2T_x$@NC. High-resolution XPS spectra of (c) Ti 2p, (d) Mo 3d and (e) N 1 s of Mo_2C/$Ti_3C_2T_x$@NC. The Ti 2p survey of pristine $Ti_3C_2T_x$ MXene is presented in (c) for comparison. The inset in (e) is the calculated contents of pyridinic N, pyrrolic N and graphitic N in Mo_2C/$Ti_3C_2T_x$@NC.

Ti $2p_{1/2}$ and Ti $2p_{3/2}$, as shown in Fig. 3c. Typically, the Ti $2p_{3/2}$ components at 454.3, 455, 456.1, and 457.8 eV are assigned to Ti–C (Ti$^+$), Ti–X (Ti^{2+}), Ti$_x$O$_y$ (Ti^{3+}), and TiO$_2$ (Ti^{4+}), respectively.[22] Compared to the pristine $Ti_3C_2T_x$ MXene, the binding energy of Ti–C positively shifts by about 0.3 eV, indicating the electron transfer from $Ti_3C_2T_x$ to Mo_2C nanodots in the hybrid.[26] The deconvoluted Mo 3d XPS spectrum (Fig. 3d) reveals that the peaks at 228.8 eV and 231.9 eV are attributed to Mo_2C. Meanwhile, due to inevitable surface oxidation, the peaks at 229.6, 232.5, 233, and 235.8 eV stem from Mo^{4+} 3d$_{5/2}$, Mo^{6+} 3d$_{5/2}$, Mo^{4+} 3d$_{3/2}$ and Mo^{6+} 3d$_{3/2}$, respectively.[33] As shown in Fig. 3e, the deconvolution of the N1s XPS spectrum reveals the peaks at 398.6, 400.5 and 401.8 eV, which could be assigned to pyridinic, pyrrolic and graphitic N, respectively. Accordingly, the content is determined to be 71.64%, 18.43% and 9.93%, respectively. The C 1 s spectrum (Fig. S8†) was fitted with five components at 282, 284.6, 285.5, 287.1, and 289.1 eV, stemming from Ti–C, C–C, C–N, C–O, and –COO, respectively. Upon comparison, the XPS spectra of Mo_2C@NC are similar to those of Mo_2C/Ti_3C_2-T_x@NC (Fig. S9†). The above XPS analyses imply that Mo_2C nanocrystals are intensely coupled on $Ti_3C_2T_x$ MXene and encapsulated in the pyridinic N-rich carbon layer.

The HER performance of Mo_2C/$Ti_3C_2T_x$@NC was evaluated by investigating the polarization curves in 0.5 M H_2SO_4 with all the potentials converted to the reversible hydrogen electrode (RHE). For comparison, Mo_2C@NC, $Ti_3C_2T_x$@NC and commercial 20 wt% Pt/C catalyst were also measured. As shown in Fig. 4a, the commercial 20 wt% Pt/C exhibits the best activity

with an onset overpotential of zero. Mo_2C/$Ti_3C_2T_x$@NC shows a low onset overpotential of 6 mV vs. RHE (Fig. S10a†), which is very comparable to that of Pt/C but much lower than that of Mo_2C@NC (53 mV) and $Ti_3C_2T_x$@NC (432 mV). Impressively, Mo_2C/$Ti_3C_2T_x$@NC shows better performance than Pt/C at higher overpotentials (>106 mV). To elucidate the HER mechanism, Tafel plots of these catalysts were calculated based on the Tafel equation $\eta = a + b \log|j|$, where j represents the current density and b is the Tafel slope.[39] As shown in Fig. 4b, the Tafel slope of Mo_2C/$Ti_3C_2T_x$@NC is determined to be 40 mV dec^{-1}, close to that of Pt/C (31 mV dec^{-1}), and lower than those of Mo_2C@NC (67 mV dec^{-1}) and $Ti_3C_2T_x$@NC (113 mV dec^{-1}). The value implies that the HER operates through the Volmer–Heyrovsky mechanism on Mo_2C/$Ti_3C_2T_x$@NC.[40] The exchange current density (j_0) for these catalysts was determined by fitting the linear portion of the Tafel plots at low current density (Fig. S10b†).[41] As displayed in Fig. 4c, the j_0 value of Mo_2C/Ti_3-C_2T_x@NC is 0.52 mA cm^{-2}, smaller than that of Pt/C (0.841 mA cm^{-2}) but much higher than those of Mo_2C@NC (0.127 mA cm^{-2}) and $Ti_3C_2T_x$@NC (2.6 × 10^{-5} mA cm^{-2}), indicating the superior intrinsic activity of Mo_2C/$Ti_3C_2T_x$@NC. To achieve a current density of 10 mA cm^{-2}, the overpotentials of 27, 53, 121, and 631 mV are required for Pt/C, Mo_2C/$Ti_3C_2T_x$@NC, Mo_2C@NC and $Ti_3C_2T_x$@NC, respectively. As listed in Table S1,† such a low overpotential indicates that the Mo_2C/Ti_3C_2-T_x@NC exhibits one of the best HER performances among those of previously reported non-noble-metal electrocatalysts, such as MoC–Mo_2C/PNCDs,[9] MoS_2/$Ti_3C_2T_x$,[26] Co-SAC,[10] and 1T′-
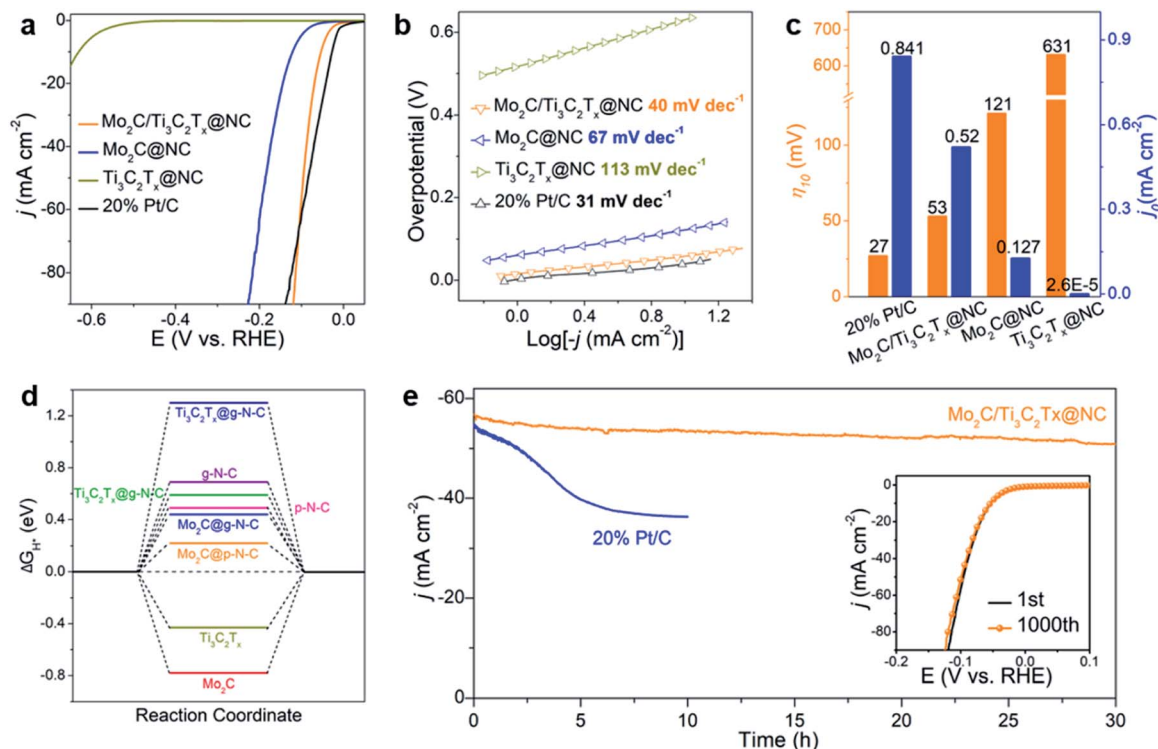
Fig. 4 (a) Polarization curves and (b) corresponding Tafel plots of Mo$_2$C/Ti$_3$C$_2$T$_x$@NC, Mo$_2$C@NC, Ti$_3$C$_2$T$_x$@NC and commercial 20% Pt/C in 0.5 M H$_2$SO$_4$. (c) Comparison of overpotentials at 10 mA cm^{-2} (η_{10}) and exchange current densities (j_0) of the four catalysts. (d) Comparison of ΔG_{H^*} of p-N-C, g-N-C, Mo$_2$C, Ti$_3$C$_2$T$_x$ as well as their heterostructures. (e) Time-dependent current density curve of Mo$_2$C/Ti$_3$C$_2$T$_x$@NC at a constant overpotential of 100 mV. The inset gives the polarization curves of Mo$_2$C/Ti$_3$C$_2$T$_x$@NC initially and after 1000 CV cycles.

ReSSe QDs.[42] Moreover, Mo$_2$C/Ti$_3$C$_2$T$_x$@NC also demonstrated excellent HER performance in basic (1 M KOH) and neutral (1 M PBS) electrolytes with an overpotential of 75 and 114 mV at 10 mA cm^{-2} and a Tafel slope of 59.2 and 80.3 mV dec^{-1}, respectively, comparable to that of state-of-the-art non-noble-metal electrocatalysts (Fig. S11†).[29,43–45]

The above results imply that Ti$_3$C$_2$T$_x$ itself shows negligible HER activity but coupling of Mo$_2$C with conductive Ti$_3$C$_2$T$_x$ can modulate the morphological structure to optimize the HER activity. The Nyquist plots of the electrochemical impedance spectroscopy (EIS) responses (Fig. S12†) show a much smaller charge transfer resistance for Mo$_2$C/Ti$_3$C$_2$T$_x$@NC than that for Mo$_2$C@NC during the HER process, evidencing the faster HER kinetics due to the introduction of the conductive Ti$_3$C$_2$T$_x$ support.[46] To further understand the intrinsic origin, the electrochemical surface area (ECSA) and per-site turnover frequency (TOF) of Mo$_2$C/Ti$_3$C$_2$T$_x$@NC and Mo$_2$C@NC were typically compared. The ECSA was estimated from the electrochemical double-layer capacitance (C_{dl}) by performing cyclic voltammetry in the region from 0.2 to 0.3 V at rates varying from 10 to 100 mV s^{-1} (Fig. S13†). The ECSA of Mo$_2$C/Ti$_3$C$_2$T$_x$@NC (603.75 cm^2) is larger than that of Mo$_2$C@NC (539 cm^2), indicating that the former has a higher number of active sites. As the Ti$_3$C$_2$T$_x$@NC has very poor HER activity, the active sites should arise from Mo$_2$C. Here, we assume that all the Mo atoms in the samples are active sites, which is determined by inductively coupled plasma optical emission spectroscopy (ICP-OES). Mo$_2$C/Ti$_3$C$_2$T$_x$@NC

has a TOF of 0.246 s^{-1} at an overpotential of 100 mV (Fig. S14†), much higher than that of Mo$_2$C@NC (0.014 s^{-1}), which is comparable to those of reported non-noble-metal HER electrocatalysts, such as 3DHP-Mo$_2$C (0.045 s^{-1})[47] and CoN$_x$/C (0.39 s^{-1}).[48]

The electrochemical results reveal that Mo$_2$C/Ti$_3$C$_2$T$_x$@NC exhibits superior HER activity to that of its counterparts. To investigate the underlying mechanism, we performed density functional theory (DFT) calculations (Fig. S15–S17†). Here we considered a simple HER pathway containing three states: the initial state of H$^+$ + e$^-$, the intermediate state of adsorbed H (H*), and the final state of H$_2$ molecule.[39] The Gibbs free energy of the H* adsorption (ΔG_{H^*}) was calculated on the considered systems. Generally, a high-performance HER catalyst has a ΔG_{H^*} value close to zero.[41] Fig. 4d shows the calculated free energy diagrams for the HER. Pristine Mo$_2$C and Ti$_3$C$_2$T$_x$ MXene have a ΔG_{H^*} of -0.78 and -0.43 eV, respectively, suggesting their strong interactions with H and consequently poor HER performance. A previous study demonstrated that pyridinic N and graphitic N in carbon contribute to the HER activity of composite catalysts.[49] The modeled pyridinic N doped graphene (p-N-C) and graphitic N doped graphene (g-N-C) possess a ΔG_{H^*} of 0.49 and 0.69 eV, respectively, which implies their unfavorable interactions with H and poor HER activities. Coupling N-doped carbon with Mo$_2$C could lead to enhanced HER performance. Typically, the ΔG_{H^*} values of Mo$_2$C@p-N-C and Mo$_2$C@g-N-C were 0.22 and 0.44 eV, respectively, which were

This journal is © The Royal Society of Chemistry 2020

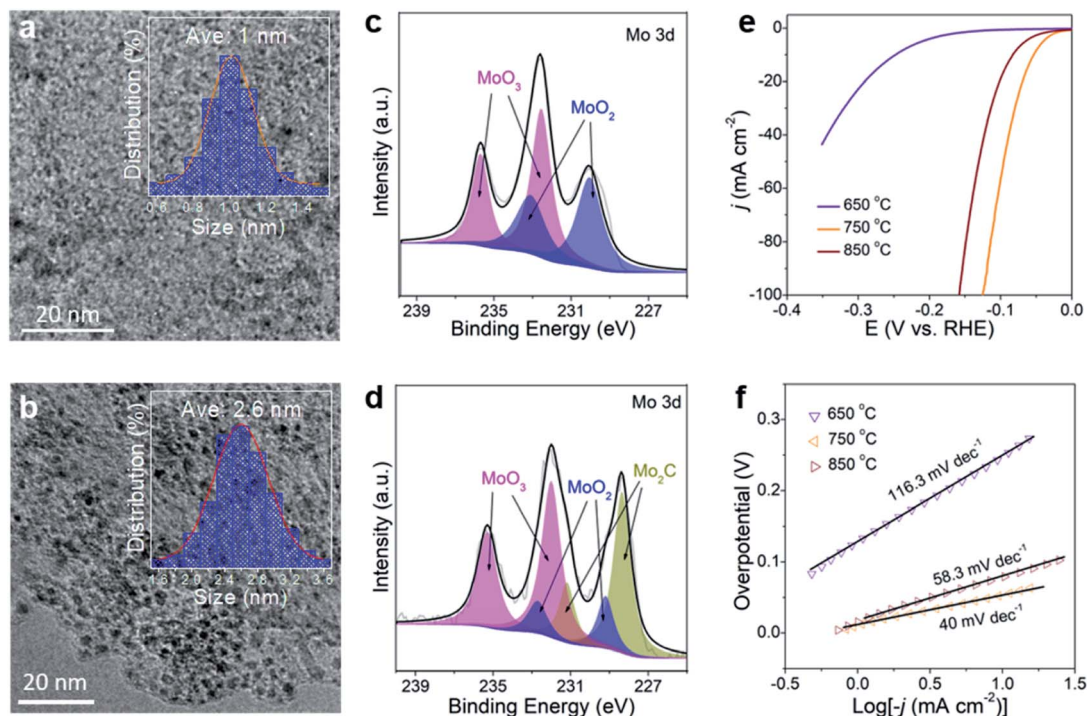J. Mater. Chem. A, 2020, 8, 7109–7116 | 7113

Fig. 5   TEM images of (a) M-650 and (b) M-850. The inset gives the size distributions of nanoparticles in the samples. High-resolution XPS Mo 3d spectra of (c) M-650 and (d) M-850. Polarization curves (e) and Tafel plots (f) of M-650, M-750, and M-850.

lower than those without N-doped carbon. Meanwhile, N-doped carbon coupled with $Ti_3C_2T_x$ MXene shows high ΔG_{H*} with unfavorable HER activity. The DFT results are in good agreement with the above experimental results, revealing that $Mo_2C@p$-N-C serves as the active sites while the MXene support facilitates the charge transfer. Notably, Chen et al.[50] reported an efficient HER catalyst of Mo single atoms anchored on N-doped carbon synthesized by an appropriate annealing method, which could be formed in the as-prepared $Mo_2C/Ti_3C_2T_x@NC$. Accordingly, the Mo–N–C active site, determined as $Mo_1N_1C_2$, is also considered. As shown in Fig. S18 and S19,† both $Mo_1N_1C_2$ and $Mo_1N_1C_2/Ti_3C_2T_x$ exhibit extremely low ΔG_{H*} values, suggesting that they are highly active toward the HER. The density of state near the Femi level for $Mo_1N_1C_2/Ti_3C_2T_x$ is higher than that of $Mo_1N_1C_2$, indicating that the $Ti_3C_2T_x$ MXenes facilitate the charge transfer during the HER process.[51]

The stability of HER electrocatalysts is also a critical indicator for practical applications. As shown in Fig. 4e, the time-dependent current density curve of $Mo_2C/Ti_3C_2T_x@NC$ at a constant overpotential of 100 mV shows a slight decrease over 30 h, which is much better than that of commercial 20 wt% Pt/C, demonstrating excellent durability. In addition, the stability of $Mo_2C/Ti_3C_2T_x@NC$ was studied using CV cycles in the range of 0.1 to −0.2 V vs. RHE. The polarization curve of $Mo_2C/Ti_3C_2T_x@NC$ after 1000 cycles (inset of Fig. 4e) shows a negligible decrease in current density compared to the initial curve, implying its long-term stability. Detailed characterization of $Mo_2C/Ti_3C_2T_x@NC$ after the stability test (Fig. S21†) further confirms the outstanding durability of its morphology and

structure, which could be attributed to the protection of the covered carbon layers.

In controlled experiments, the effect of carbonization temperature (650 °C and 850 °C) on HER performance was investigated. The samples are named M-650 and M-850. TEM images (Fig. 5a, b and S22†) reveal that MoO_x nanodots in M-650 (not completely carbonized) have an average size of 1 nm while the size of Mo_2C nanodots in M-850 is 2.6 nm. It is in good agreement with a previous report which showed that the particle size would increase with the carbonization temperature.[52] The XRD patterns of the two samples are similar to that of $Mo_2C/Ti_3C_2T_x@NC$ (here defined as M-750) except for the presence of TiO_2 signals in M-850 (Fig. S23†). The XPS results (Fig. 5c) suggest that M-650 contains MoO_x rather than Mo_2C, which could arise from the insufficient temperature. Meanwhile, as shown in Fig. 5d, M-850 has a similar Mo 3d XPS spectrum to M-750, suggesting the formation of Mo_2C nanodots. As shown in Fig. 5e, the overpotentials of M-650 and M-850 for achieving 10 mA cm^{-2} are 248 and 83 mV, respectively. And the corresponding Tafel slopes are 116.3 and 58.3 mV dec^{-1}, respectively (Fig. 5f). Obviously, M-750 exhibits the best HER activity among the three samples, which could be attributed to the following two factors: the MoO_x generated at a lower temperature (650 °C) has poorer intrinsic activity than Mo_2C, and the higher temperature (850 °C) induces aggregation of Mo_2C nanodots and partial oxidation of the MXene which would reduce the density of active sites and electron conductivity.

Based on the aforementioned considerations, the extraordinary HER performance of $Mo_2C/Ti_3C_2T_x@NC$ is postulated to

arise from the following synergistic aspects: (1) *in situ* polymerization of dopamine retains the structural stability of $Ti_3C_2T_x$ MXene at high carbonization temperature, facilitating the charge transfer; (2) polydopamine chelated MoO_4^{2-} delivers highly disperse ultrasmall Mo_2C nanodots on the surface of the MXene, favoring the high accessibility of active sites for the HER; (3) the pyridinic N dopants in carbon coupled with Mo_2C induce activated active sites for the HER; (4) the intensely coupled Mo_2C on $Ti_3C_2T_x$ provides a resistance-less path favorable for fast electron transfer; (5) the geometric confinement of Mo_2C and the MXene within the carbon layer guarantees the excellent stability of the HER performance during long-term operation.

Conclusions

In summary, we developed an *in situ* polymerization strategy to stabilize MXenes against oxidation during high-temperature treatment, which was extended to the fabrication of a hierarchical $Mo_2C/Ti_3C_2T_x$@NC composite. Serving as a HER catalyst, $Mo_2C/Ti_3C_2T_x$@NC exhibits excellent activity in the entire pH range and robust stability. Theoretical simulations demonstrated that the coupled Mo_2C and pyridinic N doped carbon serve as the most active sites for H adsorption, while the strongly incorporated metallic $Ti_3C_2T_x$ MXene provides a fast charge transfer pathway, which synergistically lead to much superior HER performance. This strategy not only provides a highly active HER catalyst, but also opens a new avenue for designing MXene-based nanocomposites that require high synthesis temperature, which could be applied in various energy-related fields.

Conflicts of interest

There are no conflicts to declare.

Acknowledgements

References

1 S. Chu, Y. Cui and N. Liu, *Nat. Mater.*, 2017, **16**, 16.

2 J. A. Turner, *Science*, 2004, **305**, 972.

3 Z. W. Seh, J. Kibsgaard, C. F. Dickens, I. Chorkendorff, J. K. Nørskov and T. F. Jaramillo, *Science*, 2017, **355**, eaad4998.

4 C. Niether, S. Faure, A. Bordet, J. Deseure, M. Chatenet, J. Carrey, B. Chaudret and A. Rouet, *Nat. Energy*, 2018, **3**, 476.

5 M. S. Faber and S. Jin, *Energy Environ. Sci.*, 2014, 7, 3519.

6 Y. Zang, S. Niu, Y. Wu, X. Zheng, J. Cai, J. Ye, Y. Xie, Y. Liu, J. Zhou and J. Zhu, *Nat. Commun.*, 2019, **10**, 1217.

7 H. Jin, X. Liu, S. Chen, A. Vasileff, L. Li, Y. Jiao, L. Song, Y. Zheng and S.-Z. Qiao, *ACS Energy Lett.*, 2019, **4**, 805.

8 H. Wang, L. Ouyang, G. Zou, C. Sun, J. Hu, X. Xiao and L. Gao, *ACS Catal.*, 2018, **8**, 9529.

9 X. F. Lu, L. Yu, J. Zhang and X. W. Lou, *Adv. Mater.*, 2019, **31**, 1900699.

10 M. D. Hossain, Z. Liu, M. Zhuang, X. Yan, G. L. Xu, C. A. Gadre, A. Tyagi, I. H. Abidi, C. J. Sun and H. Wong, *Adv. Energy Mater.*, 2019, **9**, 1803689.

11 Z. Fang, L. Peng, Y. Qian, X. Zhang, Y. Xie, J. J. Cha and G. Yu, *J. Am. Chem. Soc.*, 2018, **140**, 5241.

12 V. Jose, E. Edison, W. W. Manalastas Jr, S. Sreejith, J. M. Vianney Nsanzimana, M. Srinivasan and J.-M. Lee, *ACS Appl. Mater. Interfaces*, 2019, **11**, 39798.

13 H. Wang, Q. Yi, L. Gao, Y. Gao, T. Liu, Y.-B. Jiang, Y. Sun and G. Zou, *Nanoscale*, 2017, **9**, 16342.

14 H. Wang, X. Xiao, S. Liu, C.-L. Chiang, X. Kuai, C.-K. Peng, Y.-C. Lin, J. Zhao, J.-H. Choi, Y.-G. Lin, J.-M. Lee and L. Gao, *J. Am. Chem. Soc.*, 2019, **141**, 18578.

15 J. Yang, A. R. Mohmad, Y. Wang, R. Fullon, X. Song, F. Zhao, I. Bozkurt, M. Augustin, E. J. Santos and H. S. Shin, *Nat. Mater.*, 2019, **18**, 1309.

16 J. R. Kitchin, J. K. Nørskov, M. A. Barteau and J. G. Chen, *Catal. Today*, 2005, **105**, 66.

17 H. Wang, C. Sun, Y. Cao, J. Zhu, Y. Chen, J. Guo, J. Zhao, Y. Sun and G. Zou, *Carbon*, 2017, **114**, 628.

18 Z. Zhou, Z. Yuan, S. Li, H. Li, J. Chen, Y. Wang, Q. Huang, C. Wang, H. E. Karahan and G. Henkelman, *Small*, 2019, **15**, 1900358.

19 B. Anasori, M. R. Lukatskaya and Y. Gogotsi, *Nat. Rev. Mater.*, 2017, **2**, 16098.

20 K. Maleski, C. E. Ren, M.-Q. Zhao, B. Anasori and Y. Gogotsi, *ACS Appl. Mater. Interfaces*, 2018, **10**, 24491.

21 M. Ghidiu, M. R. Lukatskaya, M.-Q. Zhao, Y. Gogotsi and M. W. Barsoum, *Nature*, 2014, **516**, 78.

22 S. J. Kim, H.-J. Koh, C. E. Ren, O. Kwon, K. Maleski, S.-Y. Cho, B. Anasori, C.-K. Kim, Y.-K. Choi and J. Kim, *ACS Nano*, 2018, **12**, 986.

23 W. Bao, X. Tang, X. Guo, S. Choi, C. Wang, Y. Gogotsi and G. Wang, *Joule*, 2018, **2**, 778.

24 F. Shahzad, M. Alhabeb, C. B. Hatter, B. Anasori, S. M. Hong, C. M. Koo and Y. Gogotsi, *Science*, 2016, **353**, 1137.

25 J. Zhang, Y. Zhao, X. Guo, C. Chen, C.-L. Dong, R.-S. Liu, C.-P. Han, Y. Li, Y. Gogotsi and G. Wang, *Nat. Catal.*, 2018, **1**, 985.

26 J. Liu, Y. Liu, D. Xu, Y. Zhu, W. Peng, Y. Li, F. Zhang and X. Fan, *Appl. Catal., B*, 2019, **241**, 89.

27 X.-D. Zhu, Y. Xie and Y.-T. Liu, *J. Mater. Chem. A*, 2018, **6**, 21255.

28 D. Zhao, Z. Chen, W. Yang, S. Liu, X. Zhang, Y. Yu, W.-C. Cheong, L. Zheng, F. Ren, G. Ying, X. Cao, D. Wang, Q. Peng, G. Wang and C. Chen, *J. Am. Chem. Soc.*, 2019, **141**, 4086.

29 X. Wu, S. Zhou, Z. Wang, J. Liu, W. Pei, P. Yang, J. Zhao and J. Qiu, *Adv. Energy Mater.*, 2019, **9**, 1901333.

This journal is © The Royal Society of Chemistry 2020

J. Mater. Chem. A, 2020, **8**, 7109–7116 | 7115

30 X. Wu, Z. Wang, M. Yu, L. Xiu and J. Qiu, *Adv. Mater.*, 2017, **29**, 1607017.

31 J.-S. Li, Y. Wang, C.-H. Liu, S.-L. Li, Y.-G. Wang, L.-Z. Dong, Z.-H. Dai, Y.-F. Li and Y.-Q. Lan, *Nat. Commun.*, 2016, **7**, 11204.

32 H. Huang, J. Cui, G. Liu, R. Bi and L. Zhang, *ACS Nano*, 2019, **13**, 3448.

33 Y. Huang, Q. Gong, X. Song, K. Feng, K. Nie, F. Zhao, Y. Wang, M. Zeng, J. Zhong and Y. Li, *ACS Nano*, 2016, **10**, 11337.

34 M. Han, X. Yin, X. Li, B. Anasori, L. Zhang, L. Cheng and Y. Gogotsi, *ACS Appl. Mater. Interfaces*, 2017, **9**, 20038.

35 M. Yu, S. Zhou, Z. Wang, J. Zhao and J. Qiu, *Nano Energy*, 2018, **44**, 181.

36 X. Wang, Z. Wang, M. Zhang, X. Jiang, Y. Wang, J. Lv, G. He and Z. Sun, *J. Alloys Compd.*, 2017, **725**, 1166.

37 Y. Yang, M. Luo, Y. Xing, S. Wang, W. Zhang, F. Lv, Y. Li, Y. Zhang, W. Wang and S. Guo, *Adv. Mater.*, 2018, **30**, 1706085.

38 J. Zhang, L. Zhou, Q. Sun, H. Ming, L. Sun, C. Wang, Y. Wu, K. Guan, L. Wang and J. Ming, *Chem.–Eur. J.*, 2019, **25**, 8813.

39 Y. Li, H. Wang, L. Xie, Y. Liang, G. Hong and H. Dai, *J. Am. Chem. Soc.*, 2011, **133**, 7296.

40 T. F. Jaramillo, K. P. Jørgensen, J. Bonde, J. H. Nielsen, S. Horch and I. Chorkendorff, *Science*, 2007, **317**, 100.

41 J. K. Nørskov, T. Bligaard, A. Logadottir, J. Kitchin, J. G. Chen, S. Pandelov and U. Stimming, *J. Electrochem. Soc.*, 2005, **152**, 23.

42 Z. Lai, A. Chaturvedi, Y. Wang, T. H. Tran, X. Liu, C. Tan, Z. Luo, B. Chen, Y. Huang and G.-H. Nam, *J. Am. Chem. Soc.*, 2018, **140**, 8563–8568.

43 X. Zhang, X. Yu, L. Zhang, F. Zhou, Y. Liang and R. Wang, *Adv. Funct. Mater.*, 2018, **28**, 1706523.

44 I. K. Mishra, H. Zhou, J. Sun, F. Qin, K. Dahal, J. Bao, S. Chen and Z. Ren, *Energy Environ. Sci.*, 2018, **11**, 2246.

45 K. Liang, S. Pakhira, Z. Yang, A. Nijamudheen, L. Ju, M. Wang, C. I. Aguirre-Velez, G. E. Sterbinsky, Y. Du and Z. Feng, *ACS Catal.*, 2018, **9**, 651.

46 J. Liang, C. Ding, J. Liu, T. Chen, W. Peng, Y. Li, F. Zhang and X. Fan, *Nanoscale*, 2019, **11**, 10992.

47 H. Ang, H. Wang, B. Li, Y. Zong, X. Wang and Q. Yan, *Small*, 2016, **12**, 2859.

48 H.-W. Liang, S. Brüller, R. Dong, J. Zhang, X. Feng and K. Müllen, *Nat. Commun.*, 2015, **6**, 7992.

49 X. Wang, A. Vasileff, Y. Jiao, Y. Zheng and S. Z. Qiao, *Adv. Mater.*, 2019, **31**, 1803625.

50 W. Chen, J. Pei, C.-T. He, J. Wan, H. Ren, Y. Zhu, Y. Wang, J. Dong, S. Tian, W.-C. Cheong, S. Lu, L. Zheng, X. Zheng, W. Yan, Z. Zhuang, C. Chen, Q. Peng, D. Wang and Y. Li, *Angew. Chem., Int. Ed.*, 2017, **56**, 16086.

51 M. Yu, S. Zhou, Z. Wang, J. Zhao and J. Qiu, *Nano Energy*, 2018, **44**, 181.

52 Y. Liu, G. Yu, G. D. Li, Y. Sun, T. Asefa, W. Chen and X. Zou, *Angew. Chem., Int. Ed.*, 2015, **54**, 10752.

7116 | *J. Mater. Chem. A*, 2020, **8**, 7109–7116

This journal is © The Royal Society of Chemistry 2020